NANO MICRO small

Rutile Nanorod/Anatase Nanowire Junction Array as Both Sensor and Power Supplier for High-Performance, Self-Powered, Wireless UV Photodetector

Xin Yu, Zhenhuan Zhao, Jian Zhang, Weibo Guo, Jichuan Qiu, Deshuai Li, Zhou Li, Xiaoning Mou, Linlin Li, Aixue Li,* and Hong Liu**

Self-powered UV photodetectors based on TiO_2 nanotree arrays have captured much attention in recent years because of their many advantages. In this work, rutile/anatase TiO_2 (R/A-TiO_2) heterostructured nanotree arrays are fabricated by assembling anatase nanowires as branches on rutile nanorods. External quantum efficiencies as high as 90% are reached at 325 nm. These high quantum efficiencies are related to the higher amount of light harvesting due to the larger surface area, the better separation ability of the photogenerated carriers by the rutile/anatase heterostructure, and the faster electron transport, related to the 1D nanostructure and lattice connection at the interface of the two kinds of TiO_2. Furthermore, a self-powered wireless UV photodetector is shown with excellent wireless detection performance. Such devices will enable significant advances for next-generation photodetection and photosensing applications.

1. Introduction

In modern society, ultraviolet (UV) photodetectors have been widely applied in communication applications, biological and chemical analysis, environmental monitoring, remote control, memory storage, and optoelectronic circuits.[1] UV photodetectors are generally fabricated from semiconductor materials with wide bandgaps that can only absorb UV light. Some semiconductor materials can be photoexcited to produce photogenerated holes and electrons, when they are exposed to UV light. These photogenerated electrons can then be transported and flow though the outer circuit to form a current. This current is correlated with the intensity of the incident light, which is the basic principle of semiconductor-based UV photodetectors.[2] Therefore, it is critical to efficiently improve the separation and inhibit the recombination of photogenerated charge carriers to improve the sensitivity and response speed of a UV photodetector. Up to date, much effort has been made to develop different types of junctions, such as p–n junctions, p–i–n photodiodes, Schottky junctions, and metal–semiconductor–metal junctions.[3] Although these as-formed intrinsic junctions can improve the separation of photogenerated charge carriers, the photo-to-current conversion efficiency is still limited due the lack of a high enough driving force. As a result, the performance of UV photodetectors is still not satisfactory.

Self-powered nanosensors and nanosystems that can work without external power sources have been demonstrated as new approaches for pH, temperature, biomolecules, toxic pollutants, and light-detection sensors.[4] By harvesting

X. Yu, J. Zhang, W. B. Guo, D. S. Li, Prof. Z. Li, Dr. X. N. Mou, Prof. L. L. Li, Prof. A. X. Li, Prof. H. Liu
Beijing Institute of Nanoenergy and Nanosystems
Chinese Academy of Sciences
National Center for Nanoscience and Technology (NCNST)
Beijing 100083, P. R. China
E-mail: lilinlin@binn.cas.cn; liaixue@binn.cas.cn; hliu@binn.cas.cn
X, Yu, J. Zhang, W. B. Guo, D. S. Li
University of Chinese Academy of Science
Beijing 100049, P. R. China
Dr. Z. H. Zhao, J. C. Qiu, Prof. H. Liu
State Key Laboratory of Crystal Materials
Shandong University
Jinan 250100, P. R. China

DOI: 10.1002/smll.201503388

energy directly from the environment, self-powered systems will play a very important role in the independent, sustainable, maintenance-free operation of implantable biosensors, remote and mobile environmental sensors, nanorobotics, microelectromechanical systems, and even portable/wearable personal electronics.[5] In addition, the search for sustainable micro/nano-powering sources for driving wireless and mobile electronics is an emerging field in today's field of energy research, which could offer a fundamental solution to the energy needed for driving nanodevices/nanosystems.[6] Solar cells are famous for their efficiency to utilize solar light to provide a high enough voltage to drive the photogenerated charge carriers, if assembled in tandem with a photodetector.

For both solar cells and UV photodetectors, materials with excellent light-absorption capabilities are necessary. The commonly used semiconductors include TiO_2,[7] ZnO,[8] SnO_2,[9] and ZnS.[10] These materials have been widely used for solar cells and have a strong absorption in the UV-light region. Among these, nanostructured TiO_2 has been intensively studied because of its excellent physical and chemical properties, such as its high melting point, chemical inertness, direct bandgap, high photoconversion efficiency, and photostability.[11] However, TiO_2, especially granular TiO_2, generally suffers from a high recombination of the photogenerated charge carriers. This problem can be solved by utilizing well-crystallized 1D TiO_2 nanostructures, for example, nanorods, nanobelts, and nanowires.[12] Structural defects, which tend to act as trap centers for photogenerated charge carriers, are significantly reduced in 1D TiO_2 nanostructures and hence faster charge transportation is expected.

It has already been demonstrated that 1D TiO_2 nanorods are excellent candidates for UV photodetectors.[13] The advantages of TiO_2 nanorod arrays, which can be facilely grown in situ on various transparent conductive substrates, include a large surface area, fast charge transport, and improved light absorption due to the light scattering. However, one of the most important drawbacks is the poor charge separation in single-phase TiO_2 nanorod arrays. Forming junctions by assembling a secondary nanostructure has been demonstrated to be an effective solution to overcome this critical issue. By employing this strategy, at least two advantages are to be expected, including improved interfacial charge separation and an enlarged surface area.[14] TiO_2 mainly has four different crystalline phases, of which rutile and anatase TiO_2 have been investigated the most.[15] Both rutile TiO_2 and anatase TiO_2 have wide bandgaps and are excellent UV-light absorbers. The energy level of the conduction band of rutile TiO_2 is usually lower than that of anatase TiO_2 with similar energy levels of their valence band, leading to a narrower bandgap of rutile TiO_2 compared to that of anatase TiO_2. This energy difference can typically be used for charge separation, whereby the photogenerated electrons flow between the conduction band of rutile and that of anatase, if a junction is formed by rutile/anatase TiO_2. In fact, junctions formed by different phases of the same semiconductor material with identical chemical composition can be defined as phase structures and these have been widely investigated.[16] For example, photocatalysts with phase structures have aroused substantial interest as they can deliver a much higher activity than that of a single phase catalyst.[17]

Tree-like TiO_2 nanostructures grown directly on a fluorine-doped tin oxide (FTO) substrate have been widely used as the photoanode in dye-sensitized solar cells and UV photodetectors, and high photo-to-current conversion efficiencies have been achieved.[18] In these reports the branches and the trunk of the nanotrees were both rutile TiO_2. Although branch-like TiO_2 nanowires have been shown to enhance light absorption, having both parts of the heterostructure of the same crystal phase did not enhance the effective separation of the photogenerated carriers. It is therefore expected that the synthesis of TiO_2 nanotrees with different crystal phases of branches and trunks would be an ideal approach to assemble solar-cell powered UV photodetectors. Up to now, such nanotree arrays for self-powered photodetectors or solar cells have not been reported.

Here, we report on the synthesis of novel rutile TiO_2 nanorod/anatase TiO_2 nanowires (R/A-TiO_2) that form nanotree arrays by the assembly of anatase nanowires on rutile nanorod arrays, and their application for driving UV photodetectors with self-powered wireless data transmission. Excellent self-powered photodetection behavior was seen, which is proposed to be related to the higher amount of light-absorption facets, higher carrier-transport speed, and the enhanced photogenerated carrier-separation ability derived from the R/A-TiO_2 heterostructure.

2. Result and Discussion

The crystalline phase of the bare TiO_2 nanorod arrays and the branched nanotree arrays was examined by X-ray diffraction (XRD), as shown in **Figure 1**. The diffraction peaks of the bare TiO_2 nanorod arrays (curve a) located at 2θ values of 36.1°, 54.3°, 62.7°, 69.0°, 69.8°, and 76.5° are well consistent with the characteristic peaks of rutile TiO_2 according to JCPDS No. 02–0494. Peaks belonging to other TiO_2 phases

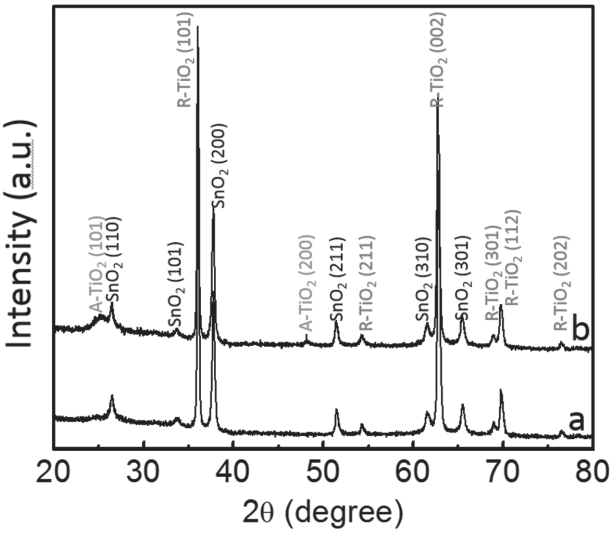

Figure 1. XRD patterns of the R-TiO_2 nanorod array (curve a) and R/A-TiO_2 heterostructures (curve b) on the FTO substrate.

were not detected, which indicates the single-crystalline feature of the rutile TiO_2 nanorods.[19] The narrow and high diffraction peaks indicate that the rutile TiO_2 nanorod arrays were highly crystalline. The diffraction peaks located at 26.5°, 33.8°, 37.9°, 51.7°, 61.7°, and 65.8° could be assigned to SnO_2 on the FTO substrate (JCPDS no. 77–0451).[20] For the nanotree arrays (curve b), the same diffraction pattern was found together with two new diffraction peaks, located at 25.3° (Figure S3, Supporting Information) and 48.0° (Figure S4, Supporting Information), which can be assigned to anatase TiO_2 (JCPDS no 21–1272).[21] The coexistence of diffraction peaks of rutile TiO_2 and anatase TiO_2 suggested that there were two crystal phases, anatase TiO_2 and rutile TiO_2, in the as-synthesized sample.

The morphology and nanostructure of the two samples were observed by scanning electron microscopy (SEM), as illustrated in **Figure 2**. Figure 2a,b shows typical SEM images of the hydrothermally grown R-TiO_2 nanorods arrays (top view) at different magnifications. It can be seen that the surface of the FTO substrate is uniformly covered with ordered TiO_2 nanorods. These TiO_2 nanorods are cubic-columnar in shape with a square top consisting of a multitude of small grids. The width of the nanorods was 50–150 nm. Combined with the XRD and SEM results, the TiO_2 nanorod array is proven to be R-TiO_2. Figure 2c,d shows the top view images of a sample prepared by a two-step synthesis on the FTO substrate. Some tiny nanowires had vertically assembled on the surface of the rutile TiO_2 nanorods to form tree-like nanostructures, and the R-TiO_2 nanorod array had turned into a nanotree array after the second synthesis step. Higher resolution observations on the samples indicated that the branches of the nanotree were about 5 nm in diameter. The R-TiO_2 nanorod formed the trunk part of the nanotree, and the anatase TiO_2 nanowires formed the branches. These anatase TiO_2 nanowires were radially grown on the R-TiO_2 nanorods. The cross-sectional view of the R-TiO_2 nanorod arrays shows that the R-TiO_2 nanorods are intimately and homogeneously grown on the FTO substrate, which should ensure fast charge transportation.[22] The cross-sectional view of the R/A-TiO_2 arrays further demonstrates the nanotree morphology, whereby the anatase TiO_2 nanowires had grown in situ on the surface of the top part of the rutile TiO_2 nanorods. The film thickness of the R-TiO_2 nanorod arrays and the R/A-TiO_2 nanotree arrays was measured to be 2.5 μm from the cross-sectional view (Figure 2e,f). Such nanotree heterostructures with the anatase TiO_2 nanowires as the outer layer can typically increase the active sites as anatase TiO_2 has a higher activity than rutile TiO_2, and the smaller size of the nanowires endow them with much more active facets.

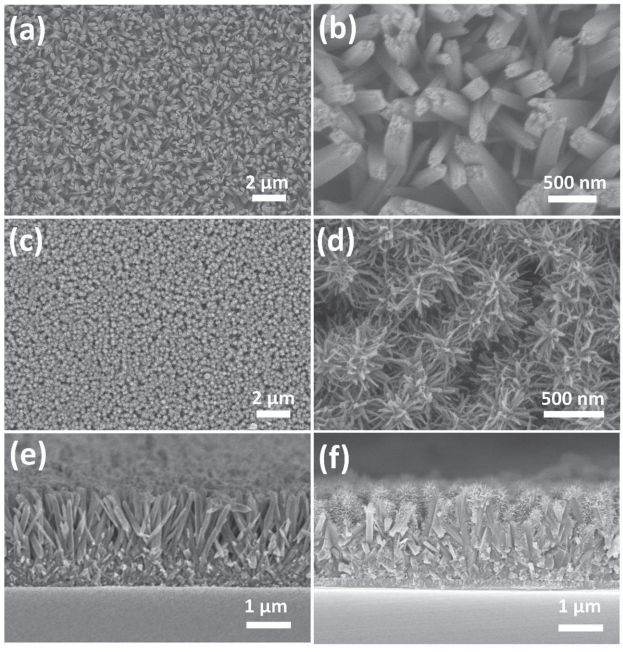

Figure 2. SEM images: a,b) top surface view of R-TiO_2 nanorods; c,d) top surface view of R/A-TiO_2 heterostructures; e) cross-sectional view of R-TiO_2 nanorods; f) cross-sectional view of R/A-TiO_2 heterostructures.

The detailed structure and crystalline lattice of the R/A-TiO_2 heterostructured nanotrees were further characterized by transmission electron microscopy (TEM) as shown in **Figure 3**. Figure 3a shows the TEM image of a typical TiO_2 nanorod, whose morphology is consistent with that observed by SEM (Figure 2b). The trunk and wire-like branches are seen to connect to form a R/A-TiO_2 heterostructured nanotree. The selected-area electron diffraction (SAED) patterns in the inset image of Figure 3a shows bright and periodic spots, indicating the single-crystalline feature of the as-prepared rutile TiO_2 nanorods, whose orientational growth was determined to be the [001] direction.[23] From Figure 3b it can be seen that a layer of TiO_2 nanowires was coated on the nanorods. In addition, from the SAED pattern an A-TiO_2 diffraction ring could be seen.[24] The high-resolution TEM images of a rutile TiO_2 nanorod and anatase nanowire in Figure 3c and d, respectively, both show clear crystalline lattice fringes, indicating a high crystallinity for both the rutile nanorods and the anatase nanowires. The measured lattice spacings for the R-TiO_2 nanorods was 3.25 Å and 2.96 Å, corresponding to the [110] crystal orientation and [001] crystal orientation of R-TiO_2, respectively. The measured lattice spacing for the A-TiO_2 nanowires was 3.52 Å, corresponding to the [101] crystal orientation of A-TiO_2. These results were consistent with the SAED results and they confirm that the nanotree heterostructure consisted of single-crystalline rutile nanorods as the trunk and anatase TiO_2 nanowires as the branch. The diameter of both the trunks and branches of the nanotree in this work were much smaller than those in previous works.[25] Most importantly, the crystalline structure of the branches and trunks in previous works were both rutile TiO_2, which caused a low photogenerated carrier-separation efficiency, and induced poor photo-electric transfer performance.

In this work, the TiO_2 nanorods were first grown on the FTO substrate with the rod axis aligned approximately perpendicular to the substrate. Oriented TiO_2 nanorod arrays could only be grown on FTO substrates. Experiments to grow TiO_2 nanorods on glass substrates were unsuccessful, indicating that nucleation and growth may require the specific epitaxy of FTO crystals. Nanorods that have nucleated and grown with their axis significantly misoriented with respect to the substrate surface normal eventually collide with a

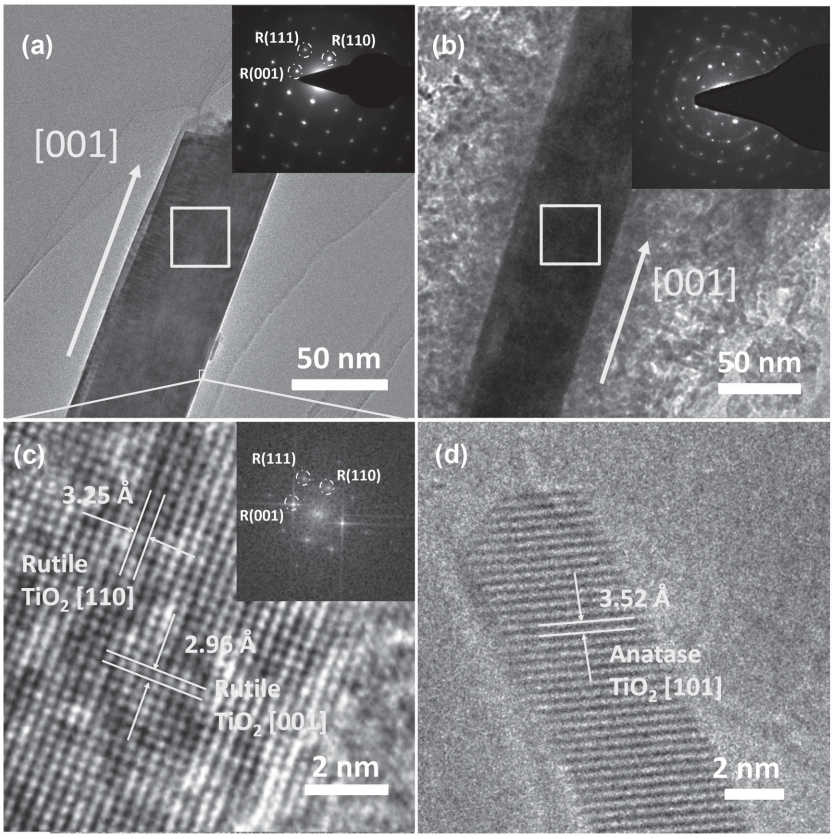

Figure 3. TEM images: a) R-TiO_2 nanorod, b) R/A-TiO_2 heterostructures, c,d) HRTEM images of R-TiO_2 nanorod (c), and A-TiO_2 nanowire (d).

neighboring nanorod and stop growing. In the next process, the formation of hierarchical anatase TiO_2 nanobranches was achieved by intelligent assembly without any assistance of a template. Through a hydrothermal reaction, the growth of the TiO_2 nanowires was achieved, and A-TiO_2 nanowire branches started to germinate on the surface of the R-TiO_2 nanorods. At this stage urea was added. The ability to retard the diameter growth rate through urea addition helped us to grow smaller TiO_2 nanowires while avoiding the side surfaces from coalescing to form a continuous film.

One of the most important properties of materials used for photodetectors is their light absorption. **Figure 4**a shows the UV–vis transmittance spectra over a wavelength range of 300 to 500 nm of the R/A-TiO_2 heterostructured nanotree and of a R-TiO_2 nanorod array. A sharp absorption edge could be observed at approximately 375 nm and 380 nm for the R-TiO_2 and R/A-TiO_2 structures, respectively. The red shift of the light absorption edge after the growth of anatase TiO_2 nanowires could be contributed to the R/A-TiO_2 heterostructures.[26] The light absorption of the R/A-TiO_2 heterostructured nanotrees was little or not weakened after the growth of the anatase TiO_2 nanowires. The low transmittance (<40%) in the wavelength range of 400–500 nm is related to the strong light scattering within the TiO_2 nanorod arrays. It may thus be concluded that the R/A-TiO_2 heterostructured nanotree is visible-blind and can only absorb UV light.

The R/A-TiO_2 heterostructured nanotree thus showed excellent light-absorption properties in the UV-light region. Therefore, the R/A-TiO_2 nanotree arrays on the FTO substrate were directly used as the photoelectrode to explore the photoelectric properties in a three-electrode set-up with Ag/AgCl and Pt plate as the reference electrode and counter electrode, respectively.[27] The recorded current density as a function of potential versus Ag/AgCl under UV-light illumination and in the dark is shown in Figure 4b. We also conducted a similar analysis of the R-TiO_2 nanorod array photoelectrode for comparison. As can be seen from Figure 4b, both the R-TiO_2 nanorod array photoelectrode and the R/A-TiO_2 heterostructured nanotree array photoelectrode showed extremely low current densities in the dark, indicating a low noise signal from the R/A-TiO_2 heterostructured nanotree as a photodetector. However, once the R-TiO_2 nanorod photoelectrode was illuminated by UV light, an anodic photocurrent occurred, which increased with increasing bias potential. The photocurrent is caused by the flowing of the photogenerated electrons through the outer circuit. The result of the photocurrent of the R-TiO_2 nanorod photoelectrode indicates that R-TiO_2 has good photoelectric properties. Surprisingly, the R/A-TiO_2 heterostructured nanotree photoelectrode showed a significantly enhanced photocurrent compared to that of the R-TiO_2 nanorod photoelectrode. The potential reason for this could be the improved charge separation and interfacial charge transfer in the heterostructure. The enhancement of photogenerated carriers can be caused by the fact that the band structure matches the separation of the induced photogenerated carriers.[28] The above results clearly show that the R/A-TiO_2 heterostructured nanotree

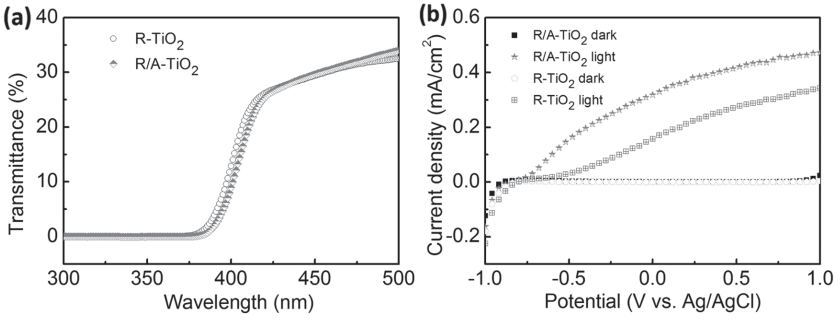

Figure 4. a) UV–vis transmittance spectra of R-TiO_2 nanorod and R/A-TiO_2 heterostructured nanotree arrays grown on FTO. b) Incident-light dependent *J–V* characteristics measured at an applied bias from –1 to 1 V under 365-nm UV-light irradiation with a light intensity of 2.0 mW cm^{-2}.

possessed excellent photoelectric properties in the UV-light region.

Based on these excellent photo-electric transfer properties, we assumed that the R/A-TiO_2 heterostructured nanotree would be an ideal candidate for UV photodetectors. Therefore, we prepared a photodetector device from the R/A-TiO_2 heterostructured nanotree array on the FTO substrate. The detailed fabrication process is elaborated in the Experimental Section. The photoelectric response was first analyzed by recording the time-dependent current under on/off switching of the UV light at 365 nm, as shown in **Figure 5**a. It was found that the photodetecting devices based on either the R-TiO_2 nanorod array or the R/A-TiO_2 heterostructured nanotree array both showed a negligible current, indicative of a low-noise feature of the photodetectors. Once the devices were illuminated by UV light, a sudden increase in the photocurrent was seen for both the R-TiO_2 nanorod photodetector and the heterostructured photodetector. Figure 5b and c show the enlarged view of a single on/off cycle of the R/A-TiO_2 heterostructured nanotree array under UV light, in which the response and the recovery time were measured to be less than 0.3 s and 0.2 s, respectively, indicating fast photoresponse features. It can clearly be seen that the photocurrent of the heterostructured photodetector was 1.8 times higher than that of the R-TiO_2 nanorod photodetector, demonstrating the higher photosensitivity of the heterostructured photodetector. In addition, no decay of the photocurrent of the photodetectors could be observed even after repeated on/off switching of the UV-light irradiation (6 times), thus showing a good stability.

The high performance of the R/A-TiO_2 heterostructured nanotree photodetector was also supported by the measured electrochemical impedance spectra (EIS). The obtained Nyquist plots of both the R-TiO_2 nanorod and R/A-TiO_2 heterostructured nanotree photodetectors are shown in Figure 5d. The EIS experiments were conducted with a frequency varying from 1000 kHz to 0.1 Hz and an AC perturbation of 10 mV under UV-light irradiation.[29] It was found that the Nyquist plots of the R-TiO_2 nanorod photodetector and R/A-TiO_2 heterostructured nanotree photodetector both

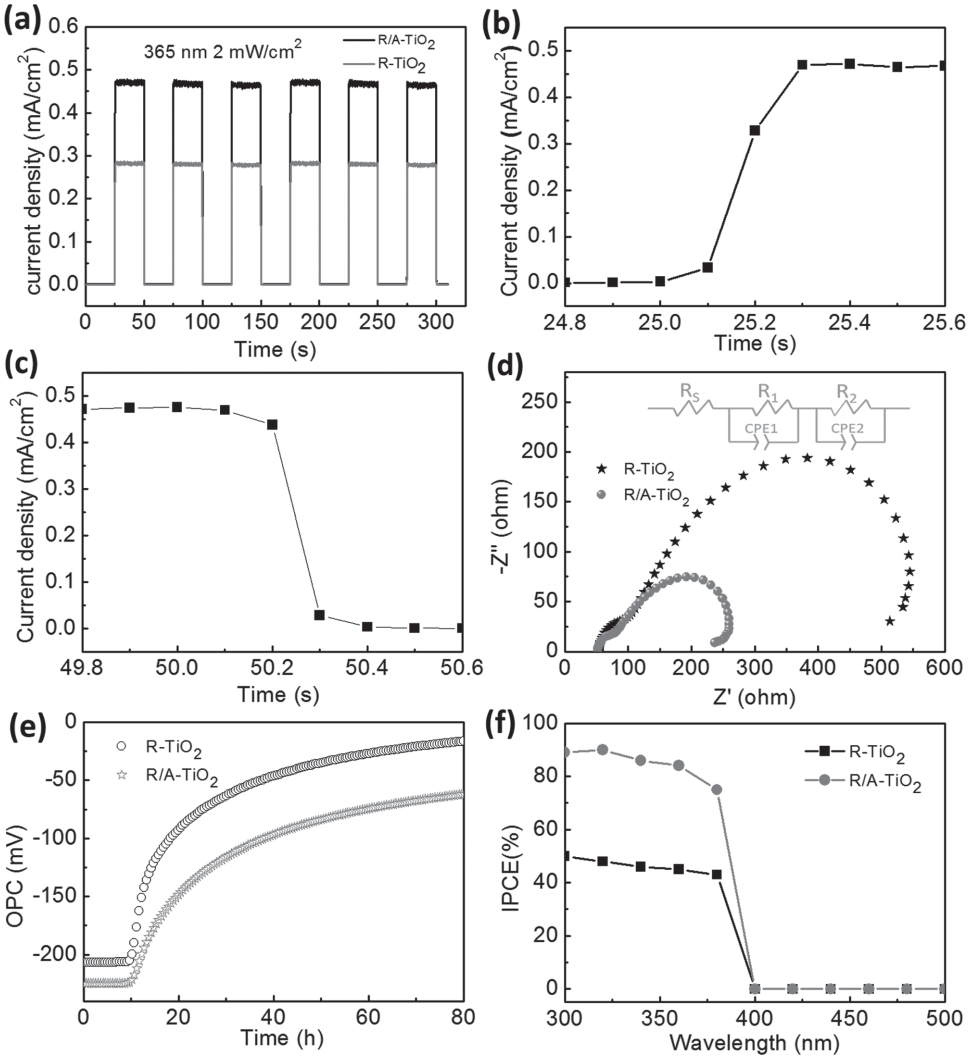

Figure 5. a) Incident-light dependent *J–t* characteristics measured with the photodetector exposed to 365-nm UV-light under on/off switching with a light intensity of 2 mW cm^{-2}. b,c) Enlarged view of a single on/off cycle of the R/A-TiO_2 photodetectors. d) EIS Nyquist plots. e) OCP as a function of time under UV light. f) IPCE spectra of R-TiO_2 and R/A-TiO_2 photodetectors.

showed two semicircles. The two semicircles are typically indicative of two charge-transfer processes.[30] The small semicircle in the high-frequency range can be ascribed to the charge-transfer process in the semiconductor depletion layer whereas the low-frequency arc resulted from electron transfer in the Helmholtz layer. The small ohmic resistance indicates the high-quality charge transfer of the as-fabricated photodetectors. The radius of the semicircle reflects the charge-transfer resistance.[31] The radius of the semicircle of the R/A-TiO_2 heterostructured nanotree photodetector was much smaller than that of the R-TiO_2 nanorod photodetector, indicating improved charge transfer in the heterostructure.

Moreover, the open-circuit potential (OCP) response of the UV photodetectors was also recorded. The OCP can reflect the lifetime of the photogenerated charge carriers in the material.[32] Under continuous irradiation, the electrons and holes will accumulate in the opposite electrodes, which increases the potential between the two electrodes in the photodetectors. As shown in Figure 5e, under continuous UV-light irradiation, the R-TiO_2 nanorod photodetector and the R/A-TiO_2 heterostructured nanotree photodetector showed stable photovoltages of about –200 mV and –220 mV, respectively. However, the photovoltages gradually decreased when the UV light was turned off. The reason for this is that the accumulated electrons flow back to the working electrode to recombine with the created holes. The rate of decrease in the OCP when the light is switched off is indicative of the lifetime of the photogenerated charge carriers. The decay of the photovoltage of the heterostructured photodetector was slower than that of the R-TiO_2 nanorod photodetector, further proving the efficient charge-separation ability of the heterostructure.

Thanks to its excellent charge separation, the R/A-TiO_2 heterostructured nanotree photodetector shows improved photoelectric properties. The incident photo-electron conversion efficiency (IPCE) of the photodetector devices was further analyzed (Figure 5f) according to[33]

$$\mathrm{IPCE} = 1240J/\lambda I_{\mathrm{light}} \quad (1)$$

where J and I_{light} are the measured photocurrent and light intensity at wavelength λ, respectively. The incident wavelength, λ, was varied from 300 nm to 500 nm at intervals of 20 nm.

In the UV-light region, the R/A-TiO_2 heterostructured nanotree photodetector displayed a high IPCE value, which was nearly twice as high as that of the R-TiO_2 nanorod photodetector, illustrating that the heterostructure has a much higher external quantum efficiency thanks to the improved charge separation in the heterostructure. The best external quantum efficiency achieved was 90% at 325 nm. This high external quantum efficiency ensures a high sensitivity of the photodetector.

The R/A-TiO_2 heterostructured nanotree photodetector was connected to a resistance to convert the current into a voltage. Then a microcontroller unit (MCU, ATmega16) was used to convert the voltage to a digital signal for self-powered wireless transmission, as shown in **Figure 6**a. We used

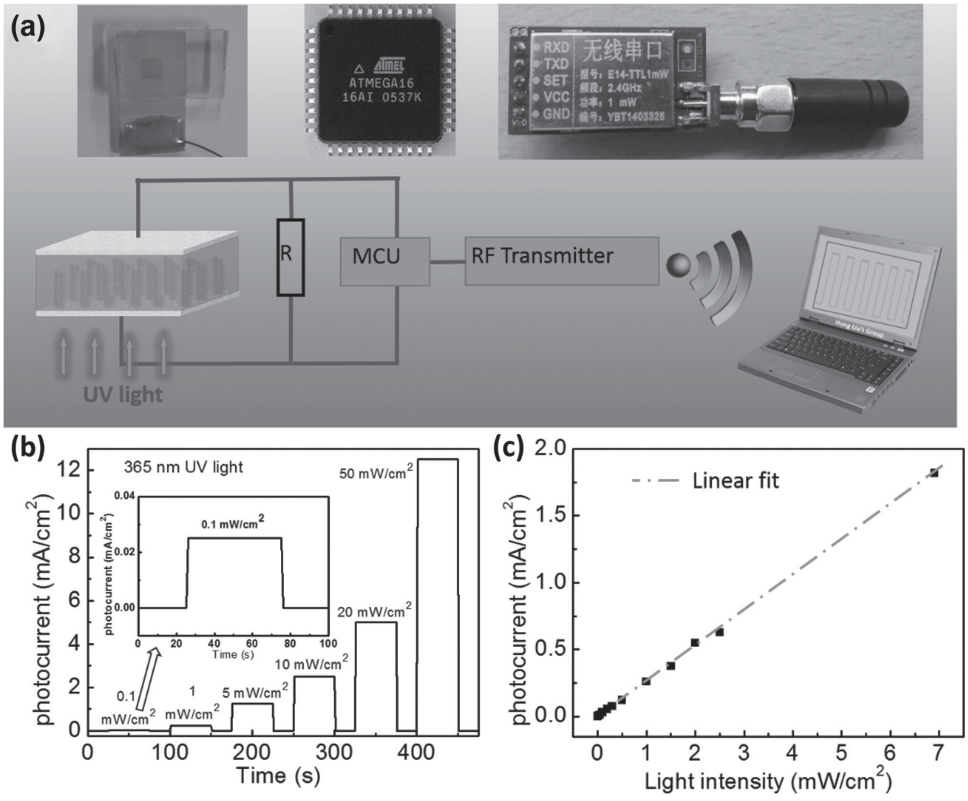

Figure 6. a) Schematic diagram of the self-powered wireless transmission device. b) Self-powered wireless data-transmission performance of the photodetector used in our self-powered wireless data transmission test. c) Photocurrent as a function of the incident UV (λ = 365 nm) intensity in a wide range from 2.5 μW cm^{-2} to 7 mW cm^{-2}.

a single transistor-radio frequency (RF, Ebyte E14-TTL1-SMA) transmitter to send out the detected digital signal. Because of the low power consumption (1 mW) of the transmitter, the energy generated by the UV detector was high enough to transmit the signal.[34] The maximum transmission distance was over 10 m. The optical images of the UV photodetector, MCU, and the RF transmitter are shown in the inset in Figure 6a. Under UV-light irradiation, the produced photocurrent flowed through the sensor, which converted the photocurrent into a wireless signal. The signal was further propagated in the form of a radio wave that could be read out by a computer. Figure 6b shows the recorded time-dependent photocurrent at different light intensities of the UV light. It can be seen that when the light intensity was set to as low as 0.1 mW cm^{-2} the photocurrent was correspondingly low but it could still be detected. Further increasing the light intensity to 1 mW cm^{-2}, obviously also increased the detected photocurrent, and the fast appearance and vanishing of the photocurrent with the on/off switching of the light indicated that the photodetector had a fast response to the UV light. Figure 6c shows the photocurrent of the R/A-TiO_2 self-powered wireless photodetector as a function of light intensity varying from 2.5 μW cm^{-2} to 7 mW cm^{-2}. The recorded photocurrent increased with increasing light intensity, exhibiting a linear relationship with the light intensity.[35] The present self-powered wireless UV photodetector showed an excellent sensitivity and fast response and still exhibited a high sensitivity even when the wireless transmission distance was as long as 10 meters. The R/A-TiO_2 heterostructured nanotree self-powered wireless photodetector is therefore very suitable for the detection in harsh environments, for instance under very strong UV-light irradiation.

The plausible mechanism behind this is illustrated in **Figure 7**a. As mentioned before, rutile TiO_2 typically has a narrower bandgap than anatase TiO_2 and the conduction-band potential (E_{CB}) of rutile (–0.05 V vs. NHE) is more positive than the E_{CB} of anatase (–0.25 V), whereas the valence band potentials are very similar.[36] Therefore, the photogenerated electrons will thermodynamically flow to the conduction band of rutile TiO_2 from the conduction band of anatase TiO_2 and the hole counterpart will flow from the valance band of rutile TiO_2 to anatase TiO_2 to form a charge flow. As the TiO_2 nanorods were grown in situ on FTO and were single crystalline the electrons in the rutile TiO_2 nanorod will be transferred fast to the FTO substrate[37] (Figure 7b). These electrons flow through the external electric circuit and arrive at the counter electrode.[38] The holes will accumulate in the valence band of anatase TiO_2, from which they can migrate to the surface of anatase TiO_2 to oxidize the I^- ions to I^{3-} ions. Moreover, the formed I^{3-} ions can be reduced to be recovered by the electrons at the Pt electrode according the reaction: $I^{3-} + 2e^- \rightarrow 3I^-$.

So the R/A-TiO_2 heterostructured nanotree arrays outperformed the bare TiO_2 nanorod arrays for four main reasons. Firstly, anatase has a higher photocatalytic activity than rutile. Secondly, compared to the TiO_2 nanorod arrays, the specific surface area and roughness of the R/A-TiO_2 nano-branched arrays were markedly enlarged, leading to an increased TiO_2/electrolyte contact area and more electron–hole pairs. Thirdly, the junction formed between rutile and anatase significantly improved the charge transfer in the heterostructure. Lastly, the good electron conductivity was retained in the vertical nanorod trunks, which enabled fast transport of the photogenerated electrons from the TiO_2

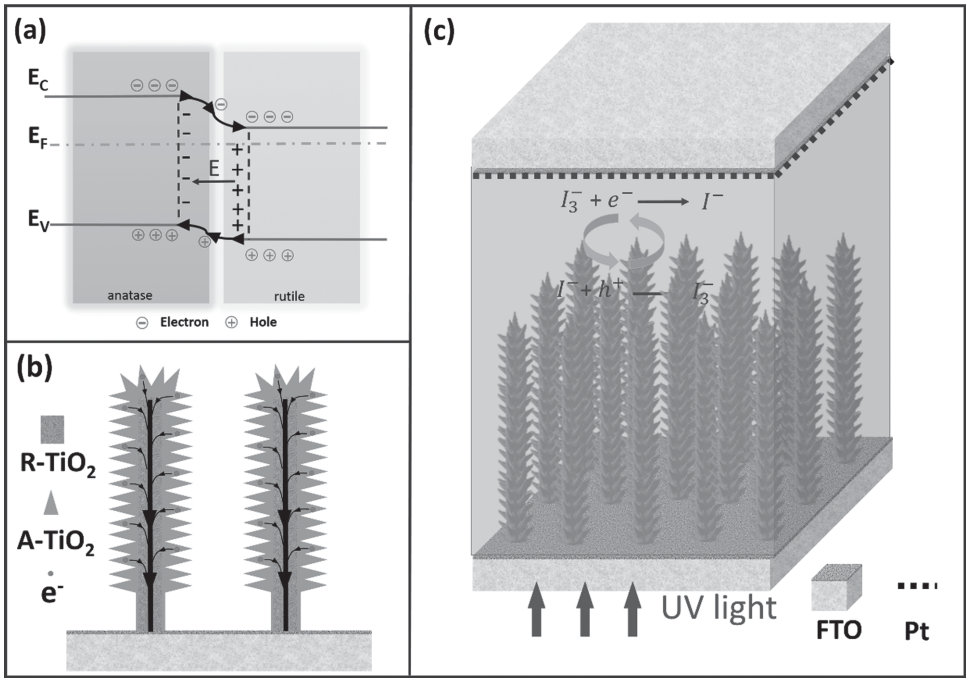

Figure 7. a) Schematic of band structures in the Z-scheme mechanism for the R/A-TiO_2 heterostructures. b) Illustrations of the electron transfer. c) The reaction in the electrolyte.

nanobranches to the collecting FTO substrate through the single-crystalline TiO_2 nanorods.

3. Conclusion

We have fabricated R/A-TiO_2 nanotree arrays with anatase TiO_2 nanowires as the branches via a simple, selective, hierarchical growth sequence and, thus, we could significantly improve the UV-light conversion efficiency. This increase in efficiency is related to the greatly augmented surface area, which enables increased light harvesting, the enhanced photogenerated carrier-separation ability, thanks to the R/A-TiO_2 heterostructure, as well as to the reduced charge recombination, because of the direct conduction along the crystalline TiO_2 nanorods. Moreover, the UV detector was successfully used to drive a sensor and wireless transmitter to realize a self-powered, wireless, real-time measurement. We believe that these R/A-TiO_2 heterostructured nanotree arrays may be useful for other applications based on the photoelectrochemical effect, such as dye-sensitized solar cells and photoelectrochemical hydrogen production, and their efficiencies may still be improved.

4. Experimental Section

4.1. Materials

All reagents in this work were analytical grade and commercially available. Titanium tetrachloride ($C_{16}H_{36}O_4Ti$), titanium oxalate $K_2TiO(C_2O_4)_2$), diethylene glycol (DEG), urea (H_2NCONH_2), ethanol (CH_3CH_2OH), acetic acid (CH_3COOH), and hydrochloric acid (HCl) were purchased from China National Medicines Corporation Ltd. Polyvinylpyrrolidone (PVP, M_w = 1 300 000) was purchased from Sigma Aldrich. All chemicals were used as received without further purification.

4.2. Method

Synthesis of R-TiO_2 Nanorods: Firstly, the R-TiO_2 nanorod arrays were prepared on FTO glass using the following hydrothermal method. A diluted hydrochloric solution was prepared by mixing 50 mL of deionized water with 50 mL of concentrated hydrochloric acid, and it was stirred at ambient temperature for 5 min. Then, 400 µL of titanium tetrachloride was added to the mixture. The solution was poured into a Teflon-lined stainless steel autoclave. The FTO substrates were ultrasonically cleaned and placed at an angle against the Teflon container wall with the conducting side facing down. The autoclave was sealed and heated to 170 °C in an oven, and held at this temperature for 6 h. After synthesis, the autoclave was cooled down to room temperature under flowing water. Then the FTO substrates were taken out, rinsed thoroughly with deionized water, and annealed at 500°C for 2 h to improve the crystallinity.

Growth of R/A-TiO_2 Heterostructured Nanotrees: A-TiO_2 branches were synthesized by a simple aqueous chemical growth method on the R-TiO_2 nanorod arrays. In a typical experiment, 0.35 g $K_2TiO(C_2O_4)_2$ and 1 g urea were added to the mixture solvent, which contained 10 mL of deionized water and 30 mL of diethylene glycol (DEG). After vigorous stirring for 30 min, the mixture solution was transferred to a 50-mL Teflon-lined stainless steel autoclave. The FTO was placed at an angle against the Teflon container wall with the R-TiO_2 side facing down. The hydrothermal synthesis was conducted at 180°C for 2 h for the growth of R-TiO_2 nanowires. The samples were then thoroughly washed with ethanol and dried in an oven at 80°C overnight. Finally, a thermal decomposition process was performed by heating the dried samples in Ar at 500°C for 2 h.

Device Fabrication: The assembly of the self-powered UV photodetector has been described in our previous work and they have the same structure as dye-sensitized solar cells, except that no dye molecules are adsorbed. In brief, the obtained TiO_2 nanobranched array electrode grown on FTO glass and the Pt counter electrode were assembled into a photoelectrochemical cell (PEC) structure. The Pt counter electrodes were prepared by depositing a 20-nm Pt film on FTO glass using magnetron sputtering. A 60-µm thick sealing material was sandwiched between these two electrodes to prevent internal short circuits. Finally, the interelectrode space was filled with a liquid electrolyte consisting of LiI (0.1 M), 1,2-dimethyl-1,3-propylimidazolium iodide (0.6 M), I_2 (0.05 M), and 4-tert-butylpyridine (0.5 M) in acetonitrile. The effective area of the UV detector was approximately 0.16 cm^2.

4.3. Characterization

XRD patterns were obtained on a Bruker D8 Advance powder X-ray diffractometer with Cu-Kα radiation (λ = 0.15406 nm).

The morphology and microstructure of the samples were examined by a scanning electron microscope (Hitachi S-8020).

The TEM images were acquired on a JEOL JEM 2100 microscope at an operating voltage of 200 kV. The samples for TEM were prepared by dropping a methanol suspension of the sample onto a copper microgrid. The sample was thoroughly dried in vacuum prior to observation.

The UV–visible transmittance spectra of the samples were recorded on a UV–vis spectrophotometer (UV-3600, Shimadzu) with an integrating sphere attachment within the range of 200 to 800 nm and with $BaSO_4$ as the reflectance standard.

A Dilor XY microspectrometer with 532-nm laser excitation was used to record the Raman spectra of the samples.

Photoelectrochemical Measurements: Photoelectrochemical analyses were carried out using a standard three-electrode cell with Ag/AgCl as the reference electrode and a Pt sheet as the counter electrode in NaOH solution (1 M). The electrolyte was bubbled with N_2 for 2 h to remove any O_2.

UV Photodetector Measurements: The device measurements were carried out using a standard two-electrode cell. Nyquist plots of the photodevices were measured at the open-circuit potential over a range of 1000 kHz to 0.1 Hz with an AC perturbation of 10 mV. The open circuit potential (OPC) response of the photodetector was recorded to give a brief idea of the recombination of the photogenerated charge carriers. Incident photon-to-current quantum conversion efficiency (IPCE) was measured using a monochromator (Newport 74004-1) and an electrochemical workstation (Gamry Reference 3000).

Self-powered Wireless UV Photodetector Measurements: the output current of the UV photodetector was measured with the aid of a laptop (Lenove China Y-450).

Supporting Information

Supporting Information is available from the Wiley Online Library or from the author.

Acknowledgements

X.Y. and Z.H.Z. contributed equally to this work. The authors are thankful for funding from the National Natural Science Foundation of China (Grant No.51402063), the China Postdoctoral Science Foundation (2014M550673), and the "100 Talents Program" of the Chinese Academy of Sciences. The authors also acknowledge the support from the "thousands talents" program for pioneer researchers and their innovation team, P. R. China.

[1] a) X. Gong, M. Tong, Y. Xia, W. Cai, J. S. Moon, Y. Cao, G. Yu, C.-L. Shieh, B. Nilsson, A. J. Heeger, *Science* **2009**, *325*, 1665; b) Q. Zhang, J. Jie, S. Diao, Z. Shao, Q. Zhang, L. Wang, W. Deng, W. Hu, H. Xia, X. Yuan, *ACS Nano* **2015**, *9*, 1561.

[2] L. Zhang, S. Bai, C. Su, Y. Zheng, Y. Qin, C. Xu, Z. L. Wang, *Adv. Funct. Mater.* **2015**, *25*, 5794.

[3] a) S. M. Hatch, J. Briscoe, S. Dunn, *Adv. Mater.* **2013**, *25*, 867; b) L. Sun, X. Wang, K. Zhang, J. Zou, Z. Yan, X. Hu, Q. Zhang, *Nano Energy* **2015**, *15*, 445.

[4] a) L. Peng, L. F. Hu, X. S. Fang, *Adv. Funct. Mater.* **2014**, *24*, 2591; b) Z. L. Wang, *Adv. Mater.* **2012**, *24*, 280; c) C.-Y. Chen, G. Zhu, Y. Hu, J.-W. Yu, J. Song, K.-Y. Cheng, L.-H. Peng, L.-J. Chou, Z. L. Wang, *ACS Nano* **2012**, *6*, 5687.

[5] a) L. Peng, L. F. Hu, X. S. Fang, *Adv. Mater.* **2013**, *25*, 5321; b) W. Wu, S. Bai, M. Yuan, Y. Qin, Z. L. Wang, T. Jing, *ACS Nano* **2012**, *6*, 6231.

[6] a) J. S. Lee, J. Oh, J. Jun, J. Jang, *ACS Nano.* **2015**, *9*, 7783; b) A. Marino, S. Arai, Y. Hou, E. Sinibaldi, M. Pellegrino, Y.-T. Chang, B. Mazzolai, V. Mattoli, M. Suzuki, G. Ciofani, *ACS Nano* **2015**, *9*, 7678.

[7] a) Y. Yin, K. Feng, C. Liu, S. Fan, *J. Phys. Chem. C* **2015**, *119*, 8488; b) P. Yan, Y. Wu, G. Liu, A. Li, H. Han, Z. Feng, J. Shi, Y. Gan, C. Li, *RSC Adv.* **2015**, *5*, 95939.

[8] a) Y. Q. Bie, Z. M. Liao, H. Z. Zhang, G. R. Li, Y. Ye, Y. B. Zhou, J. Xu, Z. X. Qin, L. Dai, D. P. Yu, *Adv. Mater.* **2011**, *23*, 649; b) C. L. Hsu, S. J. Chang, *Small* **2014**, *10*, 4562.

[9] a) X. Li, C. Gao, H. Duan, B. Lu, Y. Wang, L. Chen, Z. Zhang, X. Pan, E. Xie, *Small* **2013**, *9*, 2005; b) L. Hu, J. Yan, M. Liao, L. Wu, X. Fang, *Small* **2011**, *7*, 1012; c) S. Huang, C. F. Guo, X. Zhang, W. Pan, X. Luo, C. Zhao, J. Gong, X. Li, Z. F. Ren, H. Wu, *Small* **2015**, *11*, 5712.

[10] S. C. Rai, K. Wang, Y. Ding, J. K. Marmon, M. Bhatt, Y. Zhang, W. Zhou, Z. L. Wang, *ACS Nano* **2015**, *9*, 6419.

[11] a) K. Zheng, F. Meng, L. Jiang, Q. Yan, H. H. Hng, X. Chen, *Small* **2013**, *9*, 2076; b) Y. Xie, L. Wei, G. Wei, Q. Li, D. Wang, Y. Chen, S. Yan, G. Liu, L. Mei, J. Jiao, *Nanoscale Res. Lett.* **2013**, *8*, 1; c) Z. Wang, H. Wang, B. Liu, W. Qiu, J. Zhang, S. Ran, H. Huang, J. Xu, H. Han, D. Chen, *ACS Nano* **2011**, *5*, 8412.

[12] a) D. Zhang, F. Jing, F. Gao, L. Shen, D. Sun, J. Zhou, Y. Chen, S. Ruan, *RSC Adv.* **2015**, *5*, 83795; b) Z. Zhao, J. Tian, Y. Sang, A. Cabot, H. Liu, *Adv. Mater.* **2015**, *27*, 2557.

[13] a) L. Wang, W. Yang, H. Chong, L. Wang, F. Gao, L. Tian, Z. Yang, *RSC Adv.* **2015**, *5*, 52388; b) H. Wu, Y. Sun, D. Lin, R. Zhang, C. Zhang, W. Pan, *Adv. Mater.* **2009**, *21*, 227; c) X. Li, C. Gao, H. Duan, B. Lu, X. Pan, E. Xie, *Nano Energy* **2012**, *1*, 640.

[14] X. Wang, Q. Xu, M. Li, S. Shen, X. Wang, Y. Wang, Z. Feng, J. Shi, H. Han, C. Li, *Angew. Chem. Int. Ed.* **2012**, *51*, 13089.

[15] B. Liu, H. M. Chen, C. Liu, S. C. Andrews, C. Hahn, P. Yang, *J. Am. Chem. Soc.* **2013**, *135*, 9995.

[16] a) J. Li, M. W. G. Hoffmann, H. Shen, G. Fabrega, J. D. Prades, T. Andreu, F. Hernandez-Ramirea, S. Mather, *J. Mater. Chem.* **2012**, *22*, 20472; b) F.-X. Xiao, J. Miao, B. Liu, *Mater. Horiz.* **2014**, *1*, 259; c) D. Tsukamoto, Y. Shiraishi, Y. Sugano, S. Ichikawa, S. Tanaka, T. Hirai, *J. Am. Chem. Soc.* **2012**, *134*, 6309.

[17] a) J. Zhang, Q. Xu, Z. Feng, M. Li, C. Li, *Angew. Chem. Int. Ed.* **2008**, *47*, 1766; b) P. Yan, X. Wang, X. Zheng, R. Li, J. Han, J. Shi, A. Li, Y. Gan, C. Li, *Nano Energy* **2015**, *15*, 406.

[18] a) W. Q. Wu, H. L. Feng, H. S. Rao, Y. F. Xu, D. B. Kuang, C. Y. Su, *Nat. Commun.* **2014**, *5*, 3968; b) Y. Xie, L. Wei, Q. Li, Y. Chen, S. Yan, J. Jiao, G. Liu, L. Mei, *Nanotechnology* **2014**, *25*, 075202.

[19] X. Yu, X. Han, Z. Zhao, J. Zhang, W. Guo, C. Pan, A. Li, H. Liu, Z. L. Wang, *Nano Energy* **2015**, *11*, 19.

[20] X. Wang, Y. Sang, D. Wang, S. Ji, H. Liu, *J. Alloys Compd.* **2015**, *639*, 571.

[21] X. Yu, J. Zhang, Z. Zhao, W. Guo, J. Qiu, X. Mou, A. Li, J. P. Claverie, H. Liu, *Nano Energy* **2015**, *16*, 207.

[22] B. Liu, E. S. Aydil, *J. Am. Chem. Soc.* **2009**, *131*, 3985.

[23] Y. Wang, Y.-Y. Zhang, J. Tang, H. Wu, M. Xu, Z. Peng, X.-G. Gong, G. Zheng, *ACS Nano* **2013**, *7*, 9375.

[24] R. Chalasani, S. Vasudevan, *ACS Nano* **2013**, *7*, 4093.

[25] W. Zhou, X. Liu, J. Cui, D. Liu, J. Li, H. Jiang, J. Wang, H. Liu, *CrystEngComm* **2011**, *13*, 4557.

[26] R. Li, Y. Weng, X. Zhou, X. Wang, Y. Mi, R. Chong, H. Han, C. Li, *Energy Environ. Sci.* **2015**, *8*, 2377.

[27] G. Wang, H. Wang, Y. Ling, Y. Tang, X. Yang, R. C. Fitzmorris, C. Wang, J. Z. Zhang, Y. Li, *Nano Lett.* **2011**, *11*, 3026.

[28] G. Chen, S. Ji, Y. Sang, S. Chang, Y. Wang, P. Hao, J. Claverie, H. Liu, G. Yu, *Nanoscale* **2015**, *7*, 3117.

[29] Y. Hou, F. Zuo, A. P. Dagg, J. Liu, P. Feng, *Adv. Mater.* **2014**, *26*, 5043.

[30] W.-Q. Wu, Y.-F. Xu, C.-Y. Su, D.-B. Kuang, *Energy Environ. Sci.* **2014**, *7*, 644.

[31] a) W.-Q. Wu, B.-X. Lei, H.-S. Rao, Y.-F. Xu, Y.-F. Wang, C.-Y. Su, D.-B. Kuang, *Sci. Rep. UK* **2013**, *3*, 1352; b) J. Lin, A. Nattestad, H. Yu, Y. Bai, L. Wang, S. X. Dou, J. H. Kim, *J. Mater. Chem. A* **2014**, *2*, 8902.

[32] Y. Sang, Z. Zhao, M. Zhao, P. Hao, Y. Leng, H. Liu, *Adv. Mater.* **2015**, *27*, 363.

[33] a) T. W. Kim, K.-S. Choi, *Science* **2014**, *343*, 990; b) J. Liu, Y. Liu, N. Liu, Y. Han, X. Zhang, H. Huang, Y. Lifshitz, S.-T. Lee, J. Zhong, Z. Kang, *Science* **2015**, *347*, 970.

[34] Y. Hu, Y. Zhang, C. Xu, L. Lin, R. L. Snyder, Z. L. Wang, *Nano Lett.* **2011**, *11*, 2572.

[35] F. Zhang, Y. Ding, Y. Zhang, X. Zhang, Z. L. Wang, *ACS Nano* **2012**, *6*, 9229.

[36] Y. Cao, T. He, Y. Chen, Y. Cao, *J. Phys Chem. C* **2010**, *114*, 3627.

[37] Z. Zhao, H. Liu, S. Chen, *Nanoscale* **2012**, *4*, 7301.

[38] Y. Yu, J. Li, D. Geng, J. Wang, L. Zhang, T. L. Andrew, M. S. Arnold, X. Wang, *ACS Nano* **2015**, *9*, 564.

Received: November 6, 2015
Revised: January 9, 2016
Published online: April 7, 2016